Applied Energy 347 (2023) 121046

Contents lists available at ScienceDirect

Applied Energy

journal homepage: www.elsevier.com/locate/apenergy

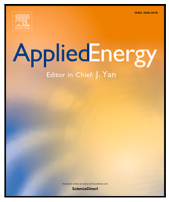

Real-time co-simulation of transmission and distribution networks integrated with distributed energy resources for frequency and voltage support

Gabriel E. Mejia-Ruiz [a], Mario R. Arrieta Paternina [a], M. Ramirez-Gonzalez [b], Felix Rafael Segundo Sevilla [b], Petr Korba [b,*]

[a] National Autonomous University of Mexico (UNAM), Mexico City, Mex. 04510, Mexico
[b] Zurich University of Applied Sciences, Winterthur, 8400, Switzerland

ARTICLE INFO

Keywords:
Distributed energy resources
Transmission-distribution co-simulation
Frequency and voltage control
Real-time simulation
Power hardware-in-the-loop

ABSTRACT

This paper proposes a real-time co-simulated framework to experimentally validate the dynamic performance of network-level controllers in power systems. The experiment setup includes the coordinated emulation of a transmission network linked to a distribution feeder and real distributed energy sources, working in a multi-platform and multi-manufacturer environment. The operation of an optimal hierarchical controller for voltage and frequency support of the transmission network, which exploits the power injection from battery energy storage systems (BESS), is investigated to demonstrate the feasibility, accuracy and effectiveness of the proposed setup based on a co-simulation environment. The results of different study cases implemented in the laboratory are presented, where a successful interconnection between real-time emulators and real hardware from different manufacturers was realised. The fast and timely response of the controller to disturbances caused by sudden load changes, three-phase faults and renewable generation losses is experimentally validated. Finally, the robustness of the developed test bench against noise and harmonic distortion of real signals is also demonstrated.

1. Introduction

Carbon emissions are the primary source of global warming. Agreements such as COP26 encourage the abandonment of fossil fuels as energy sources, promoting the massive integration of renewable power plants in modern electrical systems [1,2]. However, the high penetration of power electronics-based energy sources drastically impacts the stability and reliability of traditional control schemes on a millisecond time scale [3,4]. As a result, the development of advanced control schemes that take advantage of the capabilities and flexibility of electronic converters and energy storage systems to promptly support the grid is a growing concern for researchers and system operators [5–8].

The recent trend towards digitisation and integration of distributed energy resources in power networks has created a promising research field to analyse the impact of new actors on frequency and voltage deviations [9,10]. Actors such as smart measuring devices, multiple power sources, rapidly changing loads, new protection systems, among others, as depicted in Fig. 1. Unlike other disciplines, where impact analysis of new equipment and controllers is performed directly on real systems, testing of new assets or control strategies in electric power systems can be extremely unsafe or, in some cases, unfeasible to perform [8,11,12].

For this reason, real-time simulations (RTS) with power hardware-in-the-loop (PHIL) are a cost-effective, low-risk and highly repeatable alternative for experiments in electrical power systems [13]. This simplifies the validation process and allows parameter fine-tuning of the control architectures. Furthermore, the co-simulation between transmission and distribution networks in RT platforms with PHIL is useful to analyse critical operating conditions interacting with real hardware. However, these test environments require additional considerations for handling the non-ideal conditions, like noise and harmonic distortion, present in actual signals, which imposes additional challenges compared to offline simulations [14,15]. In this context, real-time co-simulation setups with real interaction of distributed energy resources (DERs) are imperative to better understand the short-time dynamics of modern power systems [7].

A comprehensive comparison of various real-time co-simulation approaches for transmission and distribution (T&D) networks is presented in Table 1. In [16], a simultaneous strategy for frequency support in transmission networks and voltage control in distribution feeders

* Corresponding author.
E-mail addresses: gabriel.mejia.ruiz@comunidad.unam.mx (G.E. Mejia-Ruiz), mra.paternina@fi-b.unam.mx (M.R. Arrieta Paternina), ramg@zhaw.ch (M. Ramirez-Gonzalez), segu@zhaw.ch (F.R.S. Sevilla), korb@zhaw.ch (P. Korba).

https://doi.org/10.1016/j.apenergy.2023.121046
Received 13 October 2022; Received in revised form 20 December 2022; Accepted 25 March 2023
Available online 14 June 2023

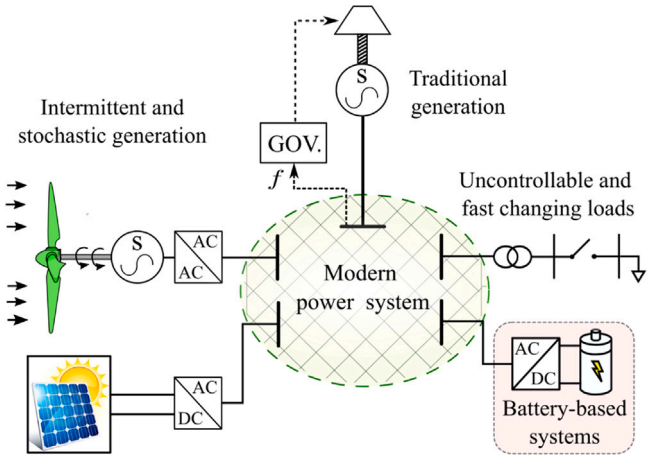

Fig. 1. Actors in the modern power systems.

is introduced taking advantage of the power injection from electric vehicles. This study includes real-time simulations with PHIL schemes. Nevertheless, the customer loads and charging stations are respectively modelled as constant loads and constant power sources, neglecting their dynamic behaviour. Experimental results exhibit large frequency excursions of up to 2.8 Hz in a 150 s time span, negatively impacting the power system stability.

From another perspective, a coordinated strategy for voltage and frequency support in distribution networks is proposed in [3] by considering battery energy storage systems (BESS). This strategy takes into account the drop-control scheme and adaptive gains. Although experimental tests at low power and low voltage are included, this strategy considers that the transmission network's frequency can be dominated by the active power injections from the distribution feeder.

Another investigation conveying experimental results of a control system based on the frequency and voltage deviations is presented in [17]. It involves numerous power sources to compensate for such imbalance. However, the controller only uses measurements at the point of interconnection of the electronic converter to the network in a fully distributed scheme, neglecting the interaction with neighbouring controllers.

The impact of large-scale battery energy storage system (BESS) integration for frequency regulation in low inertia networks is presented in [20]. This work presents control schemes in both grid-forming and grid-following modes. However, it obviates the dynamic response in a short reference frame, focusing its experiments on daily-long simulations. In [27], a primary frequency regulation control scheme in transmission networks using an adaptive state-of-charge (SOC) recovery strategy for BESSs is presented. In this proposal, the control scheme provides additional damping to enhance the virtual system's inertial ability with high PV penetration. Likewise, this work adopts the droop-type controller, but it obviates the impact of harmonic currents on the output impedance and the phase shift issues in the frequency synchronisation.

Co-simulations of distribution and transmission networks are presented in [24–26]. These works analyse the dynamic response of the grid controller; however, the impact of noise and harmonic distortion caused for real DERs in the simulation loop is disregarded. The dynamic performance analysis of transmission networks interacting with DERs is presented in [21–23]. These works preclude the distribution feeder response. A co-simulation between transmission and distribution networks is depicted in [18,19]. These investigations present static analyses with offline simulations and neglect the response of the closed-loop controller. All of these works neglect the impacts of real noise and harmonic distortion on the control system behaviour.

Given that the previously presented works have not assessed the real-time dynamic response of network-level controllers in schemes that include transmission networks, distribution feeders, and the actual interaction of DERs with the presence of noise and harmonic distortions, this investigation proposes a real-time co-simulated framework to experimentally validate the dynamic performance of control systems at the network level. This test environment includes the coordinated emulation of transmission and distribution networks interfaced with real power hardware in the simulation loop. An optimal hierarchical controller that simultaneously regulates frequency and voltage in the transmission network is applied to verify the feasibility, accuracy, and effectiveness of the proposed co-simulation environment. This controller is tested under fault conditions, sudden load changes, and the generation loss of an actual DER.

Accordingly, the most significant contributions of this work are summarised, as follows:

1. A synergistic co-simulation scheme among several hardware platforms is developed to evaluate the effectiveness of the proposed coordinated controller. In this framework, a real-time environment emulating a transmission network, a distribution feeder, and several DERs is proposed. An actual inverter and a PV emulator are interfaced with the distribution feeder model to experimentally assess the controller performance in the presence of photovoltaic generation sudden losses, noise, and harmonic distortion.
2. The proposed framework achieves the real-time implementation of an optimal hierarchical controller to simultaneously regulate frequency and voltage in transmission networks with a short response time (500 ms).
3. The fast injection of active and reactive power from the BESSs installed in different areas across the network is exploited.
4. This coordinated control approach takes advantage of a closed-loop linear quadratic Gaussian (LQG) strategy to compute the optimal active and reactive power setpoints to be injected into each area and to locally mitigate frequency and voltage excursions.
5. This framework also leverages the identification technique based on the eigensystem realization (ER) to obtain an online power network modelling and to tune the controller parameters.
6. In the control structure, an aggregator agent facilitates the computation of power setpoints for all BESSs grouped per area through their: maximum injection capacity, the SOC, and the optimal setpoints computed by the LQG controller.

The remaining sections of the work are arranged as follows. The architecture of the proposed hierarchical control scheme and the topology of the BESSs with their controllers are detailed in Section 2. Then, the theoretical foundations of the power system identification method through the eigensystem realization algorithm and the optimal LQG controller are reported in Sections 3 and 4, respectively. In Section 5, the controller performance is tested with real-time co-simulations under different scenarios involving sudden reduction of renewable energy generation, load changes and three-phase faults. Finally, concluding remarks are discussed in Section 6.

2. Real-time optimal control structure and BESS topology

The integration of distributed energy resources, digital communications and smart measurements into the network is a continuously developing research area, since the application of more interactive, distributed and flexible control strategies is a priority [5]. In this context, our investigation develops a control framework that takes advantage of smart metring architectures, battery-based storage systems and optimal controllers in each area to reduce the voltage and frequency deviations, as depicted in Fig. 2.

Table 1
Comparison of several schemes of T&D co-simulation models.

Cite	Simulation environment	Model type	Transmission network	Distribution feeder	Timeline	Controller type	Validation via
[18]	Python & OpenDSS	Static	IEEE 14-node	IEEE 8500 & EPRI Circuit 7	–	–	Off-line simulations
[19]	Matlab-Simulink™& OpenDSS	Quasi-Static	IEEE 9-node	EPRI Ckt-24 & EPRI Circuit 7	Minutes	–	Off-line simulations
[5]	Matlab-Simulink™	Dynamic	Modified Kundur 8-machine/4-area, BESSs	–	Seconds	Hierarchical coordinated controller	Off-line simulations
[17]	Matlab-Simulink™	Dynamic	1-generator 4-node, wind plant, BESS	–	Seconds	APLL-based control	RT simulations OPAL-RT
[20]	Matlab-Simulink™	Dynamic	low-inertia 10-generator and 39-node, wind plant, BESS	–	Hours	PLL-free grid-forming converter control	RT simulations OPAL-RT
[21]	Matlab-Simulink™	Dynamic	New England 10-generator and 39-node, BESSs	–	Minutes	Coordinated controller	RT simulations OPAL-RT
[22]	RSCAD	Dynamic	Modified IEEE 9-node test System with DERs	–	Seconds	Droop-based control	RT simulations RTDS
[23]	Matlab-Simulink™	Dynamic	9-node test	–	Seconds	–	RT simulations Typhoon Opal-RT
[24]	eMEGASIM & ePHASORSIM	Dynamic	European 10-node CIGRE	16-node	Seconds	–	RT simulations, OPAL-RT
[25]	ePHASORsim	Dynamic	IEEE 123-node feeder	IEEE 118-node	Hours	Volt-VAR control	RT simulations OPAL-RT
[26]	Matlab-Simulink™& RSCAD	Dynamic	European 10-node CIGRE	European CIGRE	Seconds	Centralised control strategy	RT simulations OPAL-RT RTDS
Proposed	Matlab-Simulink™, HIL control centre	Dynamic	Modified Kundur 8-machine/4-area, BESSs, solar plant	IEEE 13-node	Milliseconds	Hierarchical coordinated controller	RT simulations OPAL-RT, Typhoon, actual hardware

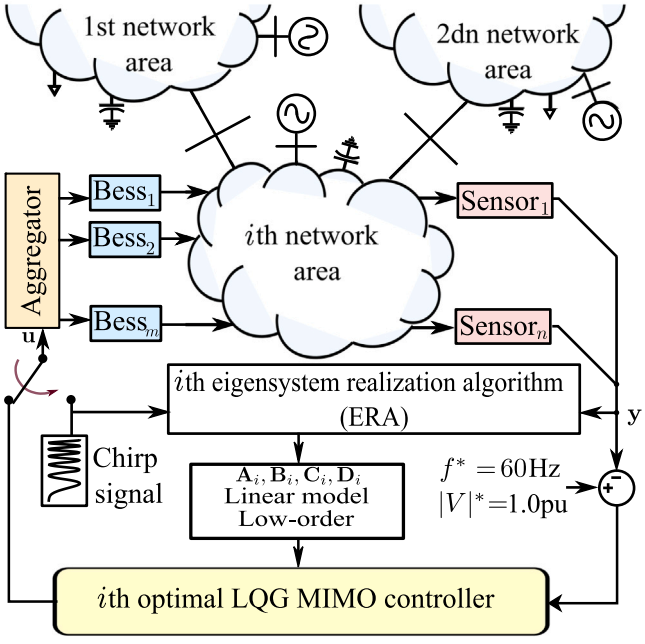

Fig. 2. Overall control diagram.

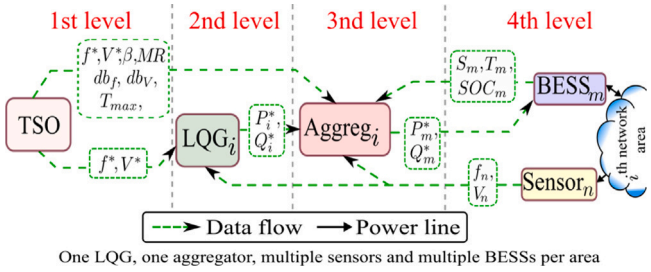

Fig. 3. Logical framework for information flow management.

The proposed approach conceives the controller separated into several subsystems according to their physical location and connections to reduce the data processing burden. Thus, the deployment of the decentralised but coordinated system includes an interactive information flow in a four-level structure, as shown in Fig. 3.

In the first level, the transmission system operator (TSO), working as a central controller, schedules network operation over a 24-h or longer horizon. Here, the TSO establishes the operating limits for voltage (db_V) and frequency (db_f), respectively; it also defines the setpoints' values as $V^* = 1$ pu and $f^* = 60$ Hz. Regarding the voltage and frequency operation, the ANSI standard provides the mandatory limits [28]. Moreover, it sets the maximum operative temperature recommended for each BESS (T_{max}). Besides, the controller in this level sends the binary command *MR* to activate the automatic identification routine of each area.

In the second level, the optimal amount of active and reactive power (P_i^* and Q_i^*) to be injected in the ith area for regulating frequency and voltage are calculated in closed-loop. In this level, the LQG controller exploits the voltage (V_n) and frequency (f_n) remote measurements acquired and streamed by nth phase measurement units (PMU) to estimate the optimal control action. The design and mathematical fundamentals of the LQG controller are presented in Section 4.

At the third level, the aggregator embeds logic rules to aggregate smartness to the controller. This aggregator works as an intermediary between the LQG controller and the BESSs installed in the corresponding area, reducing the computational task in the central controller. The flow diagram shown in Fig. 4 summarises the algorithm executed by the aggregator of each area.

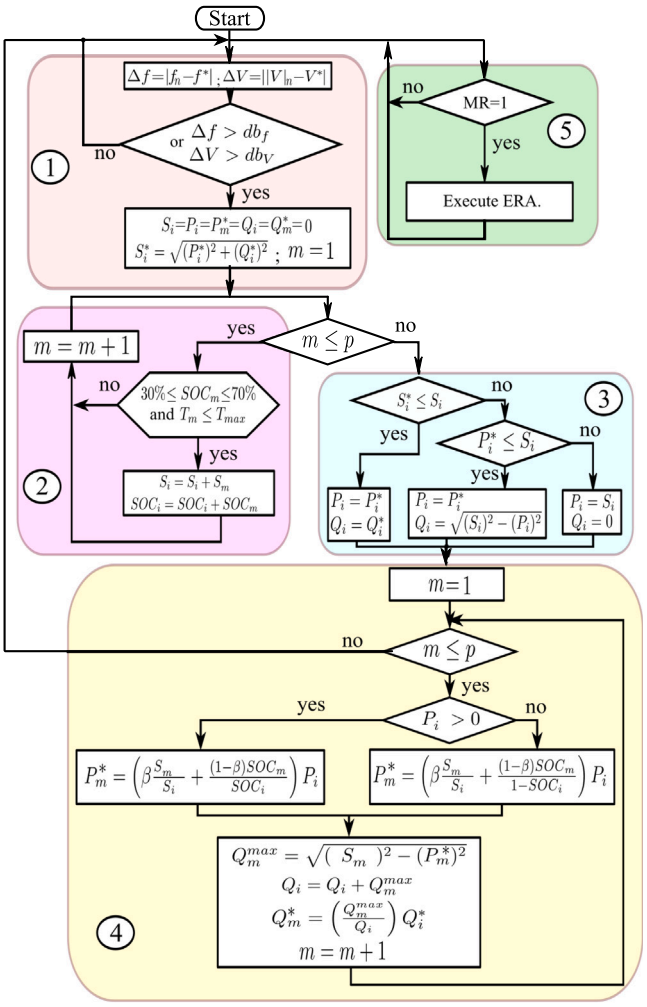

Fig. 4. Aggregator algorithm flow diagram.

In step one (highlighted in the pink box), frequency (Δf) and voltage (ΔV) deviations are estimated. Furthermore, the contingency occurrence is continuously verified. If a frequency or voltage contingency is detected, then the aggregator initialises the next variables: the available injection capacity in the area (S_i), the total active (P_i) and reactive (Q_i) powers that are requested from BESSs corresponding to the ith area, the setpoints of active (P_m^*) and reactive powers (Q_m^*) to be injected by mth BESS of the ith area, where the temporal variable m is set to one. In this step, the aggregator also computes the apparent power demanded (S_i^*) based on the optimal active power (P_i^*) and reactive power (Q_i^*) requested by the ith LQG.

In step two (highlighted in the violet box of Fig. 4), the aggregator computes S_i and the total SOC of the corresponding area (SOC_i) based on the maximum apparent power capacity (S_m) and its current SOC (SOC_m) reported for each BESS. In this step, BESSs reporting a SOC_m outside the range defined by $30\% \le SOC_m \le 70\%$ or an operating temperature (T_m) higher than T_{max} are excluded to provide ancillary services for the network, aiming to give additional protection to the BESS. m is increased in the range $1 \le m \le p$, where p is the number of BESS installed in the ith area. When $m = p$, the aggregator algorithm computes P_i and Q_i in step 3 (highlighted in the blue box of Fig. 4), in which the priority is given to the injection of active power over the reactive power injection.

In step fourth (highlighted in the yellow box), the aggregator computes P_m^* and Q_m^* based on S_m and SOC_m. In this step, the active power injection is also designated for each BESS. The TSO can prioritise the active power injection based on the SOC_m or S_m by appropriately selecting the weighting factor β ($0 \le \beta \le 1$), such weighting may be performed depending on the battery chemistry and the operational limits of the BESS.

In the aggregator algorithm, the goal of this strategy is to balance the charge or discharge of each BESS, aiming to keep the SOC close to 50%. The computation of (1) enables balancing the utilisation of all BESSs, working as follows: if $P_i > 0$, BESSs in the area must be discharged, requesting the injection of a higher amount of active power from the BESSs with the highest SOC. In contrast, if $P_i < 0$, BESSs in the area must be charged, prioritising the active power absorption towards the BESSs with lower SOC.

$$P_m^* = \begin{cases} \left(\beta\frac{S_m}{S_i}+\frac{(1-\beta)SOC_m}{SOC_i}\right)P_i & ,\forall \quad P_i > 0 \\ \left(\beta\frac{S_m}{S_i}+\frac{(1-\beta)SOC_m}{1-SOC_i}\right)P_i & ,\forall \quad P_i \le 0 \end{cases} \tag{1}$$

The automatic identification routine is executed in step five of the aggregator algorithm (highlighted in the green box). This process runs when the binary command **MR** is received from the TSO.

In the fourth level, all PMUs represent sensors, and all BESSs work as actuators of the controller structure. Each sensor sends the frequency and voltage amplitude measurements to the aggregator and LQG controller. Each BESS sends S_m^{max}, SOC_m and the operative temperature (T_m) to the aggregator. In the proposed control framework, all PMUs and BESSs may be located at different nodes of the network.

2.1. Controller and circuit of each BESS

The electronic power converter controls the bidirectional power flow between the batteries and the network at the point of common coupling (PCC). The most widely used topology is the two-level voltage source converter (VSC) detailed in Fig. 5(a). This topology allows exchanging active and reactive powers in the four quadrants of the PQ plane. The elements that compose the electronic converter are: the three switch branches that can be modelled as a controlled voltage source, the battery pack, a capacitor bank allowing to reduce the ripple at the DC side, the inductive filter on the grid side that reduces the total harmonic distortion at the AC side, and the step-up transformer for the coupling of the BESS to the high voltage grid [29].

The control system employed for each BESS is detailed in Fig. 5(b). The controller is implemented in the dq reference frame applying linear controllers, whose parameters (k_p and T_i) are tuned using the pole-localisation method and the average VSC model represented in (2) [30,31].

$$\frac{d}{dt}\begin{bmatrix} i_d \\ i_q \end{bmatrix} = L\omega \begin{bmatrix} 0 & 1 \\ -1 & 0 \end{bmatrix}\begin{bmatrix} i_d \\ i_q \end{bmatrix} + \begin{bmatrix} v_d \\ v_q \end{bmatrix} \tag{2}$$

where direct and quadrature voltages are v_q and v_d, respectively. Direct and quadrature currents are i_d and i_q. The angular speed estimation is ω and L is the inductance of the filter used in the BESS topology.

The synchronisation of the electronic converter with the grid is performed by the phase-locked loop (PLL) algorithm. i_d^* and i_q^* are calculated based on the desired active and reactive powers to be injected into the PCC (P_m^* and Q_m^*, respectively). In steady-state, the calculation of current references based on v_d can be simplified as (3).

$$i_d^* = \frac{2P_m^*}{3v_d},\ i_q^* = -\frac{2Q_m^*}{3v_d} \tag{3}$$

where i_d^* and i_q^* are the direct and quadrature setpoints for currents, respectively.

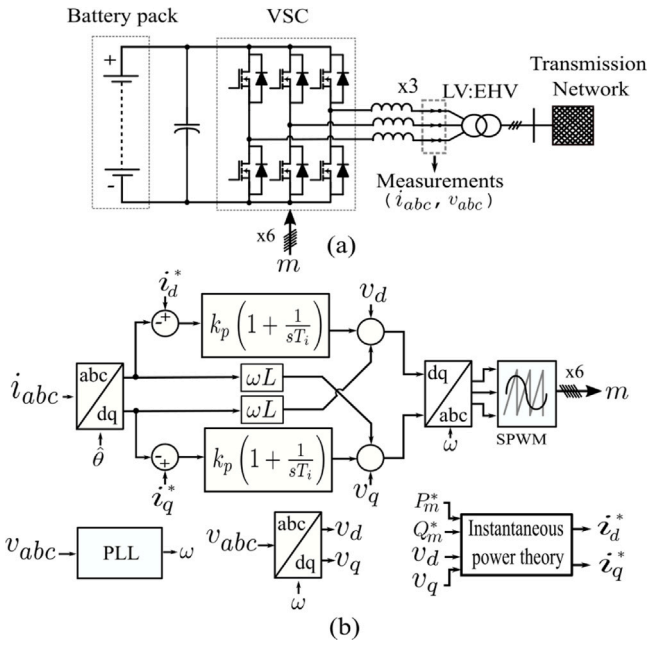

Fig. 5. BESSs' configuration. (a) Circuit topology. (b) Linear PI controllers.

3. System identification by eigensystem realization algorithm

The eigensystem realization algorithm (ERA) is a widely used method for modal identification [8,32]. The goal is to seek a minimum realisation of the state-space representation of the studied power system, such that

$$\begin{aligned}\mathbf{x}(k+1) &= \mathbf{A}_i\mathbf{x}(k) + \mathbf{B}_i\mathbf{u}(k)\\ \mathbf{y}(k) &= \mathbf{C}_i\mathbf{x}(k) + \mathbf{D}_i\mathbf{u}(k)\end{aligned} \tag{4}$$

where $\mathbf{u}(k)$ and $\mathbf{y}(k)$ stand for the input and output vectors of the identified system, respectively. The vector of the states is $\mathbf{x}(k)$ and the matrices of the linear state-space model in discrete-time are established by $\mathbf{A}_i$, $\mathbf{B}_i$, $\mathbf{C}_i$ and $\mathbf{D}_i$. The integer k is the sample indicator and i is the index of area modelled in the power system. The method for obtaining the ERA solution can be summarised in the next computational steps:

1. *To collect input and output data.* The ERA method is usually applied from the impulse response to capture the dynamics of the system to be identified. However, generating an impulse signal is impossible to achieve in practice. In this work, a pragmatic approach based on capturing system dynamics using small amplitude and easy-to-generate Chirp signals is applied. The related functions are selected to stimulate the power system dynamics, preventing system disturbances and the excitation of nonlinearities while the identification algorithm is running. Exponential Chirp functions are applied as a known input sequence ($u(k)$) to modulate the P_m^* and Q_m^* setpoint signals of the BESSs installed in the area. The low-amplitude linear Chirp function in (5) is defined as a setpoint signal.

$$u(k) = \alpha \sin\left(\frac{2\pi f_s(r_f^k - 1)}{\ln(r_f)}\right) \tag{5}$$

where f_s and f_e are the lower and upper limits of the frequency band contained in the chirp signal, α represents the amplitude, r_f is defined as $(f_e/f_s)^{1/T}$ and T is the time duration of the signal. Then, the system response is collected from the smart measurement devices in terms of the voltage amplitude ($|V|_n$) and frequency (f_n) at the same sampling rate of the setpoint signals.

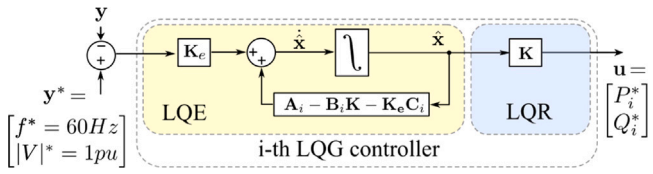

Fig. 6. LQG controller diagram.

2. *Computing the linear relationship of each input–output pair.* To obtain the transfer function as an equivalent impulse response from the chirp functions for each input and output pair, the Fourier transform is applied to each data sequence such that $\mathscr{F}(u(k))$ and $\mathscr{F}(y_q(k))$, resulting in $U(\omega)$ and $Y_q(\omega)$. The inverse Fourier transform is then applied, as follows

$$\mathbf{y}(k) = \mathscr{F}^{-1}\left(\frac{Y_q(\omega)}{U(\omega)}\right) \tag{6}$$

3. *Assembling a block-Hankel matrix.* By arranging the measured data in the following way

$$\mathbf{H}_{(k-1)} = \begin{bmatrix} \mathbf{y}_k & \mathbf{y}_{k+1} & \cdots & \mathbf{y}_{k+N} \\ \mathbf{y}_{k+1} & \mathbf{y}_{k+2} & \cdots & \mathbf{y}_{k+N+1} \\ \vdots & \vdots & \ddots & \vdots \\ \mathbf{y}_{k+N} & \mathbf{y}_{k+N+1} & \cdots & \mathbf{y}_{k+2N} \end{bmatrix} \tag{7}$$

where A^{k-1} is the transition matrix that features the system dynamics, and $\mathbf{y}_k = \mathbf{C}\mathbf{A}^{k-1}\mathbf{B}$ is the impulse responses ($\mathbf{u}_0 = 1$, $\mathbf{u}_k = 0$ for $k > 0$) of the system at time k, assuming that $\mathbf{x}_0 = 0$.

4. *Performing the singular value decomposition of* $\mathbf{H}_0$. The ERA is based on the singular value decomposition of the Hankel matrix $\mathbf{H}_{(k-1)}$ associated with the impulse response of the system.

$$\mathbf{H}_0 = \mathbf{U}\boldsymbol{\Sigma}\mathbf{V}^T \tag{8}$$

where Σ is the diagonal matrix containing the singular values of $\mathbf{H}_0$. $\mathbf{U}$ and $\mathbf{V}$ are the left and right singular vectors, respectively.

5. *Finding the right order of the system.* In this work, the order of the system is selected by quantifying 99% of the total energy of the system represented in the first singular values of the diagonal matrix Σ. Then, $\mathbf{U}$, $\mathbf{V}$ and Σ are truncated to derive a condensed representation of the power system with reduced order.

6. *Computing the discrete-time system matrices.* The matrices of the discrete-time model of the studied power system are given by

$$\begin{aligned}&\mathbf{A}_i = \boldsymbol{\Sigma}^{-\frac{1}{2}}\mathbf{U}\mathbf{H}_1\mathbf{V}^T\boldsymbol{\Sigma}^{-\frac{1}{2}};\ \mathbf{B}_i = \boldsymbol{\Sigma}^{\frac{1}{2}}\mathbf{Q}^T\\ &\mathbf{C}_i = \mathbf{P}\boldsymbol{\Sigma}^{\frac{1}{2}};\ \mathbf{D}_i = y(0)\end{aligned} \tag{9}$$

where $\mathbf{H}_1$ is the shifted block-Hankel matrix of $\mathbf{H}_0$.

4. Linear quadratic Gaussian controller design

The control scheme computes the optimal actions to minimise frequency and voltage deviations in each controlled area by reducing the error with respect to reference setpoints established by the operator. This MIMO controller also minimises the amount of energy required to reach the steady state, enhancing the BESSs operation. The design of the LQG controller is carried out following its two typical stages: the linear quadratic controller (LQR) and the linear quadratic estimator (LQE). The estimator and controller gains are computed based on the linear model obtained by the ERA method previously described in Section 3.

4.1. Linear quadratic regulator

The efficiency of the regulation is evaluated by means of a quadratic-based performance criteria defined, as follows:

$$J(\mathbf{x},\mathbf{u},\mathbf{Q},\mathbf{R}) = \int_0^\infty \left(\mathbf{x}^T\mathbf{Q}\mathbf{x} + \mathbf{u}^T\mathbf{R}\mathbf{u}\right) dt \tag{10}$$

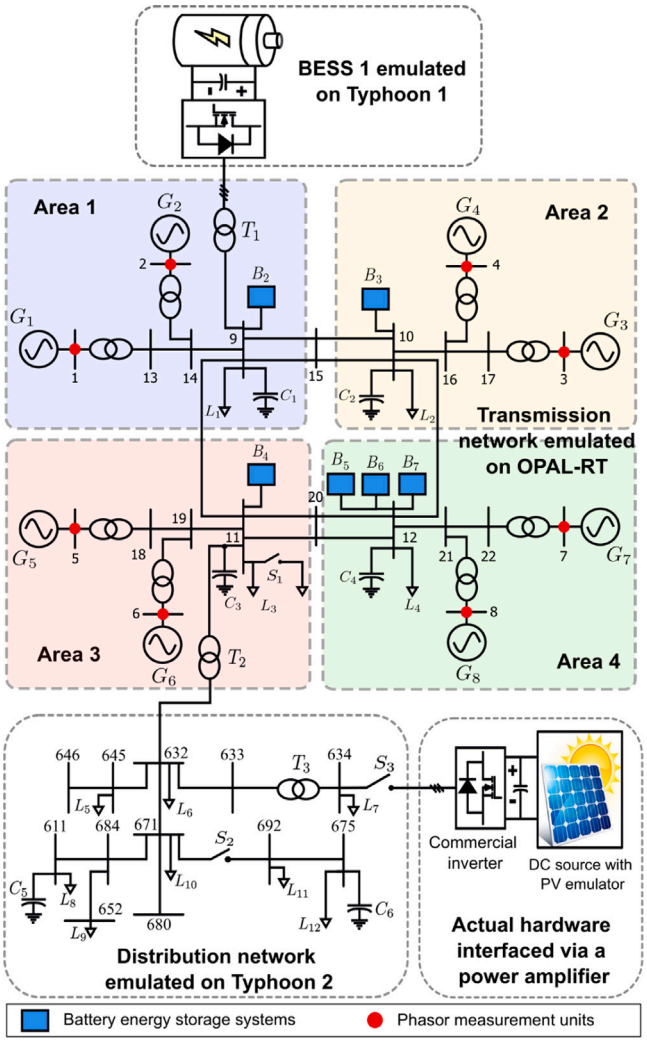

Fig. 7. Overall diagram of the real-time co-simulation testbed.

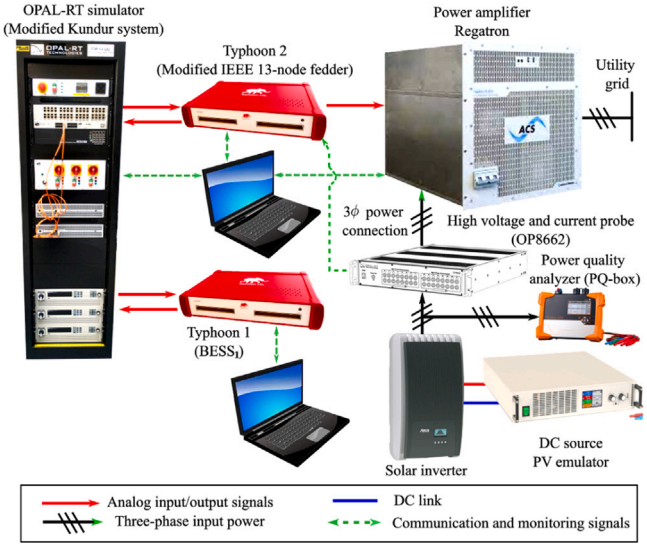

Fig. 8. Physical connections of the hardware used in the test bench.

where **Q** and **R** are the weighting matrices. These matrices are user-specified and define the trade-off between regulation performance and

Fig. 9. Photo of the experimental testbed. (1) Power amplifier. (2) OPAL-RT emulator. (3) Typhoon emulators (4) High voltage and current probe. (5) SCADA of BESS 1. (6) Power quality analyser. (7) Oscilloscope. (8) SCADA of the transmission grid and Typhoon 1 host PC. (9) Solar inverter. (10) PV emulator. (11) SCADA of the distribution grid. (12) Typhoon 2 host PC.

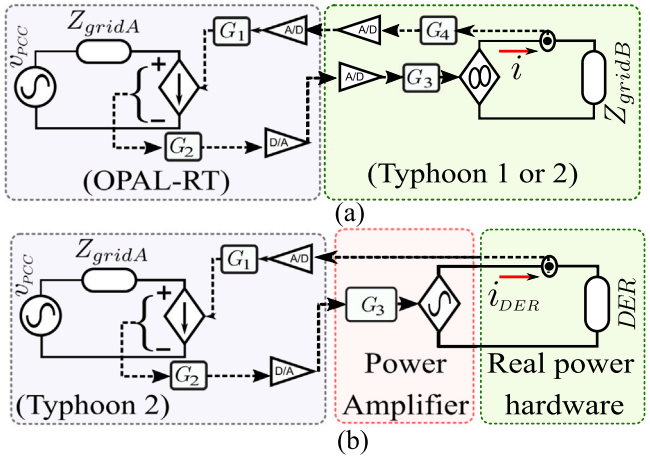

Fig. 10. Voltage-type ideal transformer model interfacing algorithm. (a) Among two power system emulators using analog signals. (b) Between an emulator and a power amplifier for power hardware-in-the-loop simulation.

control effort. The linear quadratic problem is solved by establishing a control law $\mathbf{u} = -\mathbf{K}\mathbf{x}$, such that $(\mathbf{A}_i - \mathbf{B}_i\mathbf{K})$ is stable and J is minimised. In this control law, the gain $\mathbf{K}$ optimises (10), and is expressed as:

$$\mathbf{K} = \mathbf{R}^{-1}\mathbf{B}_i^T\mathbf{P} \tag{11}$$

where $\mathbf{P}$ is obtained by solving the algebraic Riccati equation defined as follows:

$$\mathbf{P}\mathbf{A}_i + \mathbf{A}_i^T\mathbf{P} - \mathbf{P}\mathbf{B}_i\mathbf{R}^{-1}\mathbf{B}_i^T\mathbf{P} + \mathbf{Q} = 0 \tag{12}$$

4.2. Linear quadratic estimator

The sensing and processing of the full-state variables in electrical power systems are technologically unfeasible in many cases or prohibitively expensive. Nevertheless, the LQR design requires full state measurement aiming to establish the control law **u**. In that conditions, the Kalman filter allows estimating the power system state variables from the partially measured information.

The state estimator $\hat{\mathbf{x}}$ is designed such that the covariance of $(\mathbf{x} - \hat{\mathbf{x}})$ is minimised, i.e. the next index J_e must be minimised.

$$J_e = \mathbb{E}\left(\{\mathbf{x} - \hat{\mathbf{x}}\}^T\{\mathbf{x} - \hat{\mathbf{x}}\}\right) \tag{13}$$

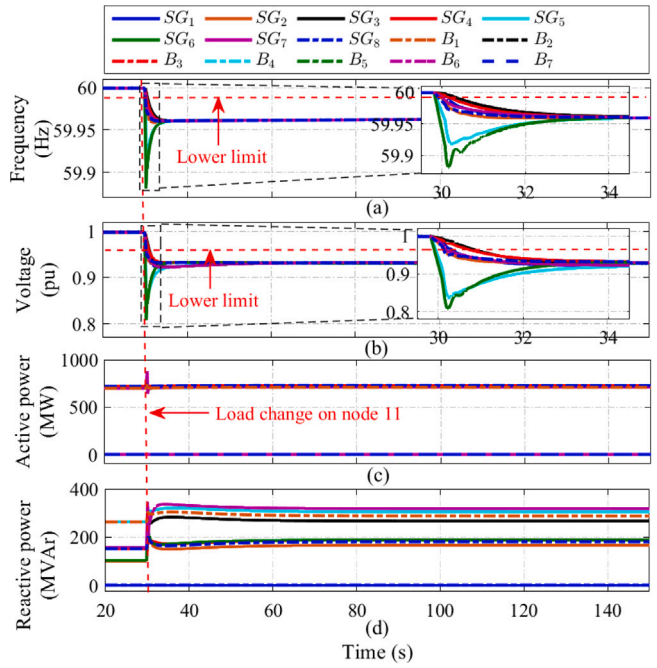

Fig. 11. Transmission network response to a sudden increase of L_3 located at bus 11 when the optimal controller is turned off (*Scenario 1*). (a) Frequency response. (b) Voltage response. (c) Active power. (d) Reactive power.

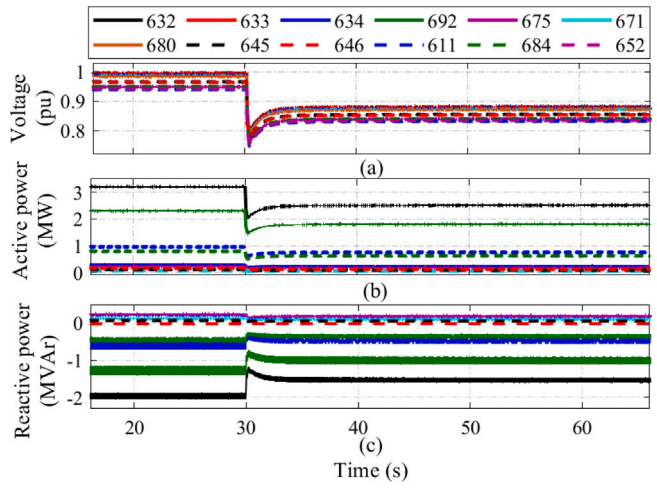

Fig. 12. Response of distribution feeder to a sudden increase of L_3 located at bus 11 when the optimal controller is turned off (*Scenario 1*). (a) Voltage response. (b) Active power. (c) Reactive power.

The system dynamics equation obtained by the state observer of the Kalman filter is given by

$$\begin{cases} \dot{\hat{\mathbf{x}}} & = \mathbf{A}_i\hat{\mathbf{x}}_i + \mathbf{B}_i\mathbf{u} + \mathbf{K_e}(\mathbf{y} - \hat{\mathbf{y}}) \\ \hat{\mathbf{y}} & = \mathbf{C}_i\hat{\mathbf{x}} \end{cases} \tag{14}$$

where $\mathbf{K_e}$ is the Kalman filter gain defined by (15).

$$\mathbf{K_e} = \mathbf{P_e}\mathbf{C}_i^T\mathbf{R}^{-1} \tag{15}$$

$\mathbf{P_e}$ is the positive definite solution of the following Riccati equation:

$$\mathbf{P_e}\mathbf{A}_i^T + \mathbf{A}_i\mathbf{P_e} - \mathbf{P_e}\mathbf{C}_i^T\mathbf{R}^{-1}\mathbf{C}_i\mathbf{P_e} + \mathbf{Q} = 0 \tag{16}$$

Thus, the closed-loop system in terms of the LQR and LQE schemes is depicted in Fig. 6.

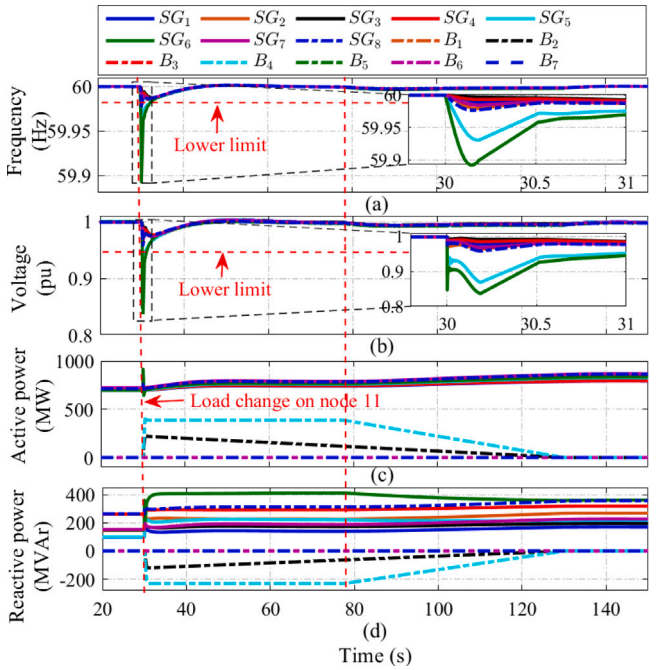

Fig. 13. Transmission network response to a sudden increase of L_3 located at bus 11 when the optimal controller is working in closed-loop (*Scenario 1*). (a) Frequency response. (b) Voltage response. (c) Active power. (d) Reactive power.

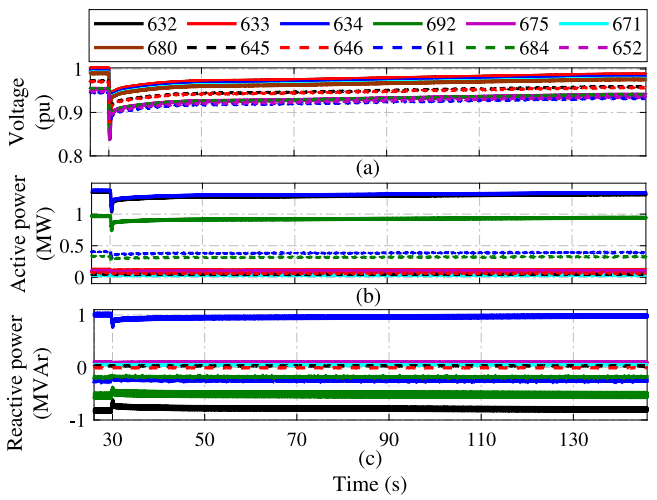

Fig. 14. Response of distribution feeder to a sudden increase of L_3 located at bus 11 when the optimal controller is working in closed-loop (*Scenario 1*). (a) Voltage response. (b) Active power. (c) Reactive power.

5. Experimental results

This section encloses the testbed system and scenarios to assess and validate the performance of the proposed real-time co-simulation environment via the implementation of the control and identification framework described in Sections 2–3.

5.1. Experimental testbed

The experimental setup is composed of a transmission network interfaced with a distribution feeder and several DERs, as shown in Fig. 7. The modified Kundur system (MKS) equipped with four interconnected areas and eight synchronous generators is used as a testbed for the transmission network. The first modification consists of interconnecting

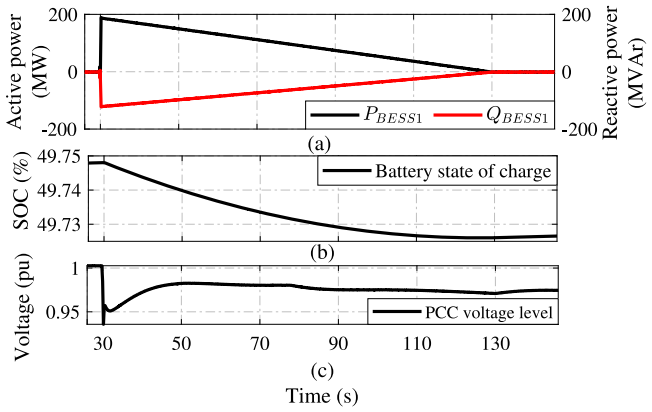

Fig. 15. RT simulation results of BESS 1 to a sudden increase in L_3 located at bus 11 (*Scenario 1*). (a) Active and reactive powers injected at bus 9. (b) Batteries' State-of-charge (SOC). (c) Voltage variation at the PCC.

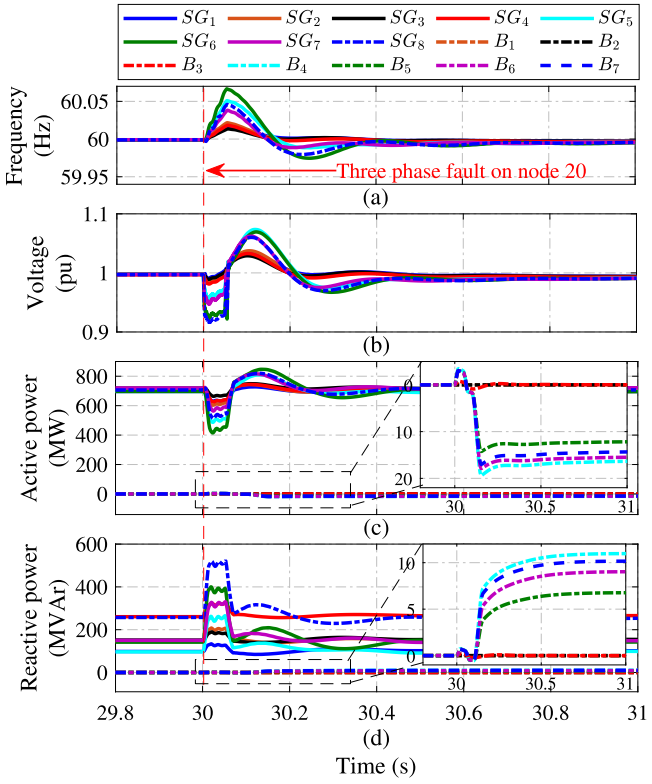

Fig. 16. Response of the transmission network when a 3-cycle three-phase fault happens at bus 20 (*Scenario 2*). (a) Frequency response. (b) Voltage response. (c) Active power. (d) Reactive power.

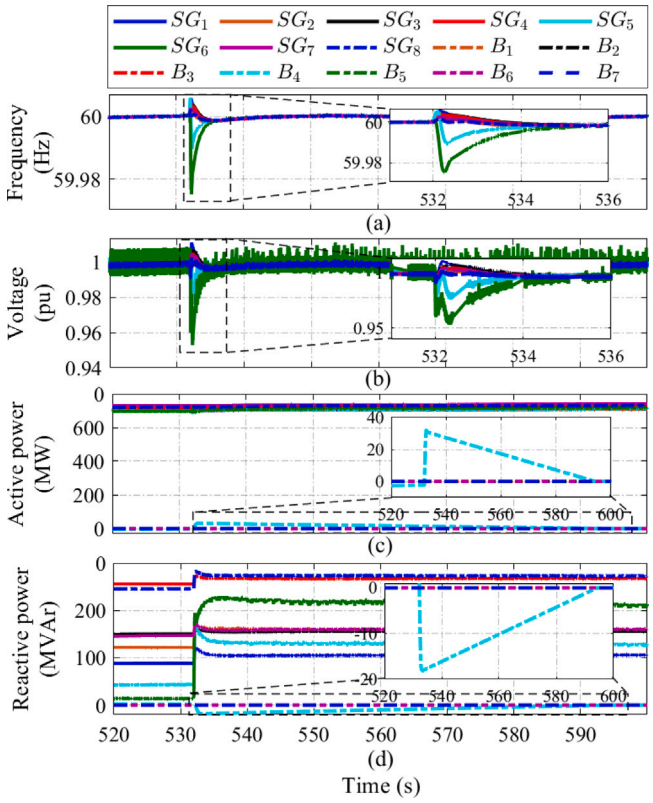

Fig. 17. Simulation results of transmission network for a sudden generation loss in the real solar plant (*Scenario 3*). (a) Frequency response. (b) Voltage response. (c) Active power. (d) Reactive power.

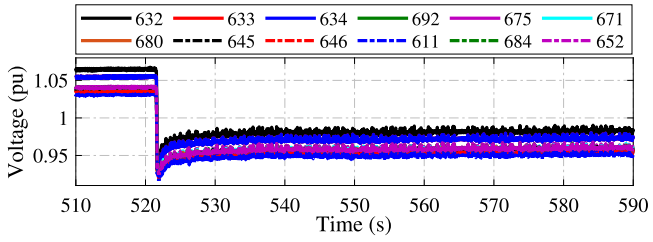

Fig. 18. Voltage response of the distribution feeder to a sudden generation loss in the real solar plant.

twice the well-known two areas Kundur system with two main tie-lines (transmission lines between nodes 9–10 and nodes 11–12) of 100 km, as seen in the middle part of the one-line diagram in Fig. 7. All synchronous generators (SGs) are modelled using a sixth-order model, whose parameters are summarised in Table 2. Each SG is controlled by its own steam turbine and governor system and its own excitation system. The governor model is implemented as a tandem-compound steam prime mover system, including a speed regulator, a steam turbine, and a shaft with a single mass; meanwhile, the exciter model is implemented as an IEEE type 1 excitation system.

The second modification comprises the interconnection of seven BESSs ($B_1 - B_7$) to the transmission level for providing reactive and active power injections; the dq-control structure and VSC-based circuitry of each BESS are shown in Fig. 5. Eight PMUs, depicted as red circles in Fig. 7, are used to sense the amplitude and frequency of the voltage used as control variables in the proposed scheme. The third change integrates the IEEE 13-node test distribution feeder to the transmission level at node 11 of the MKS through a step-down transformer T_2. This distribution grid is characterised by short lines, operating at 4.16 kV, with shunt capacitors and highly unbalanced loads. A commercial inverter-interfaced solar PV emulator is connected at node 634 via the circuit breaker S_3, as indicated on the bottom right part of Fig. 7. The detailed parameters of the distribution grid are described in [8]. The simulation parameters for all BESSs and step-down/up transformers are specified in Tables 3 and 4.

From the hardware perspective, the physical connections for all devices are shown in Figs. 8 and 9. Table 5 summarises the references of all devices. In this testbed, the transmission network, BESSs 2-7 and the hierarchical optimal controller were emulated on the OPAL-RT simulator OP5700 with 8 processor cores of up to 3.2 GHz, 16 GB of RAM and 256 I/O lines. $B_2 - B_7$ are emulated with a time step of 100 μs, using an average model that neglects the switching ripple. BESS

Table 2
SGs parameters.

All parameters in p.u.							
x_d	x'_d	x''_d	x_q	x'_q	x''_q	x_l	R_s
1.8	0.3	0.25	1.7	0.55	0.25	0.2	0.0025
All parameters in seconds					**Rated values**		
T'_{do}	T''_{do}	T'_{qo}	T''_{qo}	–	S	V_{L-L}	f
8	0.03	0.4	0.05	–	900 MVA	20 kV	60 Hz
Inertia values in seconds							
H_1		H_2		H_3		H_4	
6.5		6.5		6.175		6.175	

Table 3
Simulation parameters.

Parameter	Value
Rated voltage and battery type	1000 V, Lithium-ion
BESS grid-side inductance filter (L_g)	30 mH ×3
BESS DC-side capacitor filter (C_1, C_2)	120 μF, 200 μF
BESS controller Parameters (k_p and k_i)	k_p = 70 μ, k_i = 30 m
T_1 transformer ratio	420 V/230 kV_{rms}
T_2 transformer ratio	4.16 kV/230 kV_{rms}
T_3 transformer ratio	4.16 kV/240 V_{rms}
BESS 1 simulation time step	10 μs
Distribution grid simulation time step	50 μs
Transmission grid simulation time step	100 μs
Sampling rate and resolution of Typhoon analog-to-digital converter (ADC)	1 MHz, 16 bits
Sampling rate and resolution of OPAL-RT ADC	200 MHz, 16 bits

Table 4
BESSs parameters.

	Area 1		Area 2	Area 3	Area 4		
BESS number	1	2	3	4	5	6	7
Max. capacity (MVA)	450	450	150	450	450	400	300
Initial SOC (%)	50	50	40	40	40	60	50
Max. temp. (°C)	150	150	150	150	150	150	150
β	0.6	0.6	0.5	0.6	0.5	0.4	0.6

1, highlighted at the top of Fig. 7, is completely emulated by using a dedicated Typhoon real-time simulator, and it is interconnected via a step-up transformer T_1. A switched model with a 10 kHz switching frequency is used to emulate B_1, aiming to reproduce the effect of the switching noise in the closed loop system.

The distribution feeder and BESS 1 were emulated on two HIL402 platforms manufactured by Typhoon, each one with 4-core and 96 I/O lines. Besides, a solar-based DER is emulated through the real inverter StecaGrid 3203 of 3.2 kW and the PV emulator PSI9500. The actual photovoltaic system is interfaced with the HIL402 emulator through a full 4-quadrant 3-phase AC power amplifier Regatron TC.ACS of 30 kVA.

All real-time dynamic models of the transmission network, BESSs 2-7, and the hierarchical controller are implemented in the Matlab & Simulink™ environment with the RT-LAB libraries provided for the OPAL-RT emulator. The distribution feeder and BESS 1 are implemented in a HIL control centre platform for Typhoon emulators.

Numerous algorithms can facilitate interfacing hardware platforms for real-time simulation of different manufacturers and with actual hardware via power amplifiers. Among these, the voltage-type ideal transformer model is widely used and represents a straightforward implementation. It also has high accuracy and high stability [15,33]. This model is implemented to emulate the power transfer from BESS 1 towards the transmission system and from the distribution feeder towards the transmission network, as depicted in Fig. 10(a). On the OPAL-RT side, the voltage measurements at the PCC (V_{PCC}) are scaled to the range ±10 V using G_2. The resulting signals are converted from digital to analog. On the typhoon side, the voltage signals are transformed from analog to digital. The resulting signal is scaled by G_3 to reproduce the corresponding voltage levels at the PCC. These signals are also filtered in G_3 to reduce their bandwidth, increasing the stability of the connection loop. The currents through the PCC are represented by controlled current sources, whose controlled signal stems from the measurements at the PCC on the typhoon side. Such signals are also filtered and scaled using G_3 and G_4, respectively. This algorithm emulates in real-time the power transfer between the modelled power systems between OPAL-RT and the two typhoons, respectively.

Table 5
Hardware used for assembling the testbed.

System	Reference
Transmission system emulator	OPAL-RT OP5700
BESS 2-7 emulator	OPAL-RT OP5700
Distribution system emulator	Typhoon HIL402
BESS 1 emulator	Typhoon HIL402
Power amplifier	Regatron TC.ACS.30.528 30 kVA
Solar inverter	StecaGrid 3203 3.2 kW/3 × 230 V
DC source, PV Emulator	PSI 9500-10-06-2U 1.5 kW/500 V
High voltage and high current probe	OP8662
Power quality analyser	PQ-BOX 200

Similarly, the distribution feeder can also be interfaced with actual power hardware using a power amplifier, as shown in Fig. 10(b). The gains G_{1-3} scale and filter the signals. The power amplifier reproduces three-phase unbalanced voltages at node 634. In this scheme, Z_{gridA} and Z_{gridB} represent the impedances at the PCC of the simulated power systems.

5.2. Test scenarios

The optimal control structure and the proposed multi-platform emulation testbed are verified under the following scenarios, evidencing the precision and timely response of the controller, as well as the stability and robustness of the communication links among emulation platforms and real power hardware.

Scenario 1: it compares the open-loop and closed-loop performance of the MKS (transmission level). The control systems operate in response to a load increase of 130% at node 11. The load change is presented at 30 s, closing the breaker S_1 in Fig. 7. The governor and excitation controllers of all SGs remain active and the breaker S_3 is open in both simulations.

Scenario 2: the performance and robustness of the proposed controller are tested in the presence of a 3-cycle three-phase-to-ground fault at bus 20 of the MKS. The power system stabiliser (PSS), governor and excitation controllers work together with the proposed optimal controller, acting in a closed loop. The network parameters remain at their rated values.

Scenario 3: the performance of the proposed controller is evaluated to promptly and timely reduce the frequency and voltage deviations in the transmission system caused by a solar generator's sudden loss connected at bus 634 of the distribution grid, as shown in Fig. 7. The robustness of the proposed hardware configuration and controllers is validated in the presence of real noise and harmonic distortion injected from the solar inverter. The power injected by the solar inverter is amplified 10 000 times to produce an observable change in the transmission network. The active power is reduced with a step change from 50 MW to 0 MW.

5.3. Results

Results in scenario 1: an exhaustive comparison of the power system dynamic response when the proposed controllers work in open-loop and closed-loop is accomplished in response to a load increase at bus 11. For instance, the behaviour of the transmission network and

distribution feeder is respectively depicted in Figs. 11 and 12. With the optimal controller switched off, notice that the sudden load change produces fast excursions in frequency and voltage at all measured buses, and those deviations are below the established lower limits db_f and db_V, marked with the red dotted line in 11(a) and Fig. 11(b), respectively. The contingency causes a transitory increase of active power, as shown in Fig. 11(c). In addition, this contingency also provokes an increase in reactive power at all monitored nodes, which remains with magnitudes higher than the nominal values, as shown in Fig. 11(d).

The response of the distribution feeder in *Scenario 1* is displayed in Fig. 12. It is remarkable how the contingency yields voltage drops lower than 0.9 pu at all nodes, as depicted in Fig. 12(a). Under these conditions, the system operates outside the safe limits established in the standard ANSI C84.1 (below 0.95 pu) [28]. Likewise, Fig. 12(b) shows the reduction of the active power supplied to the fixed resistive loads of the distribution feeder. The reactive power absorbed at all nodes changes, reacting to the significant drop in the power delivered, as shown in Fig. 12(c).

In contrast, when the hierarchical optimal controller is operating in closed-loop and the contingency described in *Scenario 1* takes place, the control system activates the BESSs in the neighbourhood areas to precisely and promptly alleviate voltage and frequency deviations, as shown in Fig. 13(a) and (b). When the contingency is detected in area 3, the corresponding LQG controller computes the optimal active and reactive power required to reduce the disturbance. The local aggregator computes the power setpoints for the BESSs grouped in area 3 according to the algorithm in Fig. 4, saturating the setpoints in the pre-established operating limits for B_4. Considering the limited injection capacity of B_4, the contingency spreads to area 1, activating B_1 and B_2, as depicted in Fig. 13(c) and (d). The power supplied by all the activated BESSs drives the frequency and voltage within the preset deadbands (db_f and db_V) and closes to the reference values ($f^* = 60$ Hz and $|V|^* = 1$ pu) in less than 2 s. Simultaneously, the aggregator computes a setpoint reduction in a ramp form, granting enough time for the SGs to assume the necessary supply to compensate for the load change. At 77 s, the setpoint reduction for B_4 is equal to the ramp computed by the aggregator, and the power injection triggers its reduction until reaching zero at 128 s (see Fig. 14).

The response of BESS 1 to the load change at bus 11 is exhibited in Fig. 15. Notice that the active and reactive powers injected at bus 9, Fig. 15(a), correspond to 188 MW and −121 MVAr, and are calculated by the optimal control system and the aggregator. Subsequently, the power injection is ramped down to zero. The BESS is initially operating with a SOC of 50% and injects active power for about 2 min. In this period, the energy stored by the batteries is reduced to 49.73%, as shown in Fig. 15(b). The voltage at the BESS's PCC with the network is also reduced to 0.98 pu, remaining within the safe limits established by the ANSI standard [28], as depicted in Fig. 15(c).

Results in scenario 2: to verify the robustness and reliability of the experimental testbed and the proposed framework, the system response to a three-phase to ground fault at bus 20 is presented in Fig. 16. At 30 s, the fault is triggered causing significant frequency and voltage excursions at all monitored nodes, as shown in Fig. 16(a)–(b). The detected voltage and frequency disturbances are comparatively higher at the closest nodes to the point of fault occurrence, i.e. nodes 5-8. The proposed controller reacts to promptly reduce the frequency and voltage deviations by injecting active and reactive power from the BESSs in areas 3 and 4 of the transmission network ($B_4 - B_7$). BESSs installed in areas 1 and 2 ($B_5 - B_7$) are not involved in the network support process in this scenario, because the voltages and frequencies measured between the db_V and db_f established limits, as shown in Fig. 16(c)–(d).

The effects of the fault are completely mitigated and the steady state is attained in less than 2 s. After that, all the power injected by the BESSs is reduced in ramp form.

Results in scenario 3: the response of the proposed control system to the presence of a 50 MW sudden generation loss in the solar plant is illustrated in Fig. 17. In this scenario, the solar inverter's power injection at bus 634 of the distribution grid is amplified up to 50 MW. At 532 s, the generation is reduced to 0 W in a step-wise way, evidencing frequency and voltage excursions below the db_f and db_V established limits, as shown in the zoomed areas of Fig. 17(a)–(b), respectively. Besides, the voltage measurements at the nodes of SG_5 and SG_6 show a high-frequency voltage ripple of ± 2% caused by the commutation of the power switches in the actual inverter and the noise coupled in the cables used for communication of the measuring equipment in the actual power system. The proposed LQG controllers reject the noise, acting as a low-pass filter.

In response to the disturbance, B_4 is activated initiating active and reactive power injections to compensate for the loss of generation, as shown in the enlarged areas of Fig. 17(c)–(d). Subsequently, the power injection of B_4 is ramped down given time for the SGs to assume the generation until the steady state is reached at 63 s after initiating the regulating action.

The voltage response in the distribution feeder to the presence of a sudden generation change in the emulated solar plant connected at bus 634 is presented in Fig. 18. The voltage increases 6% at all nodes of the distribution feeder, such increment is above the nominal value when a 5 MW active power is injected into the transmission grid at node 632. However, when the generation changes, then the grid voltage suddenly decreases, achieving the nominal values of the utility grid.

The proposed controller reduces frequency and voltage variations, even in the presence of highly unbalanced voltages/currents conditions. Actual polluted signals allow the verification of the noise tolerance in the proposed testbed. The voltage and current measurements at the point of connection between the solar inverter to the grid and the power amplifier are shown in Figs. 19 and 20. The voltage node emulated by the power amplifier is highly unbalanced, reproducing the features of the distribution feeder at node 634. In these conditions, the voltages measured per phase are 254 Vrms, 234 Vrms, 213 Vrms, respectively.

Figs. 19 and 20 depict the three-phase voltage and three-phase current at the coupling point between the actual inverter and the power amplifier, without applying any filter to the three-phase current signals and with the filter applied, respectively. Fig. 19 shows the result of the coupling of high-frequency noise from the commutation of the power switches and the harmonic distortion from the three-phase current to the three-phase voltage at the point of connection between the PV inverter and the power amplifier. This electrical noise impacts the stability of the interaction between the power amplifier and the distribution feeder model running on the Typhoon 2 emulator, constraining the amplification of the power generated by the PV plant. Under these conditions, the harmonic distortion in the three-phase voltage at the PCC increases to 23.9%. The application of a low-pass filter to the three-phase feedback current with a cutoff frequency of 1 kHz reduces the bandwidth and enhances the stability of the connection, significantly reducing the high-frequency noise coupling and harmonic distortion in the voltage at the connection point, as is shown in Fig. 20.

6. Conclusions

The penetration of distributed energy resources into modern power grids is gradually growing, advocating the exploitation of these new resources for the provision of ancillary services largely depends on the studies and knowledge that can be achieved in controlled test environments. In this context, a multi-platform real-time simulation with actual power hardware enables the analysis of stability, reliability and effectiveness of novel control, protection and cyber-security strategies. This paper presents a real-time co-simulation of a transmission system interfaced with a distribution network, battery energy storage systems and an actual solar generator. This is conducted in a symbiotic way that includes multiple platforms from multiple manufacturers and power

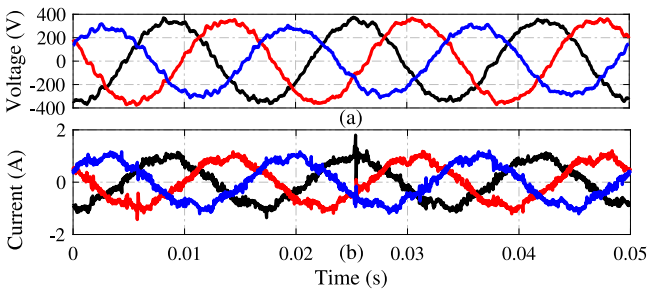

Fig. 19. Measurements at the PCC with the PV inverter without low-pass filtering of the feedback currents. (a) Three-phase voltage. (b) Three-phase current.

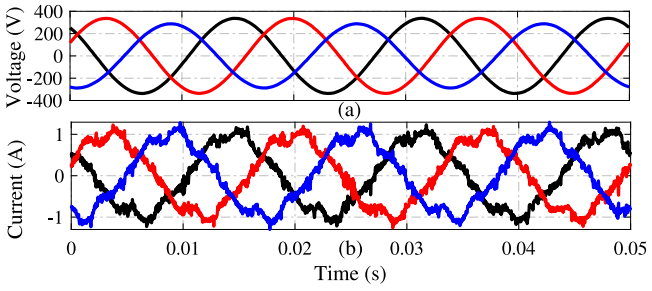

Fig. 20. Measurements at the PCC with the PV inverter with a low-pass filter of the feedback currents (cut-off frequency 1 kHz). (a) Three-phase voltage. (b) Three-phase current.

hardware-in-the-loop. This testbed is applied to verify the effectiveness of an optimal hierarchical controller for frequency and voltage regulation in the transmission network.

Experimental results demonstrated that the proposed hardware setup is effective for the real-time emulation of the power system dynamic behaviour integrated with transmission and distribution networks. The proposed control system regulates frequency and voltage with accuracy, even in the presence of real electrical noise, harmonic distortion, and significant changes in the operating point of the system. The dynamic performance and stability of the entire system are maintained despite the occurrence of events such as three-phase faults, sudden generation losses and load changes of up to 130%, evidencing the reliability and robustness of the proposed framework.

CRediT authorship contribution statement

Gabriel E. Mejia-Ruiz: Conceptualization, Methodology, Formal analysis, Writing – original draft, Investigation, Visualization, Software. **Mario R. Arrieta Paternina:** Supervision, Investigation, Data curation, Writing – review & editing. **M. Ramirez-Gonzalez:** Data curation, Writing - review & editing. **Felix Rafael Segundo Sevilla:** Proofreading. **Petr Korba:** Proofreading.

Declaration of competing interest

The authors declare that they have no known competing financial interests or personal relationships that could have appeared to influence the work reported in this paper.

Data availability

No data was used for the research described in the article.

References

[1] Kim J, Bialek S, Ünel B, Dvorkin Y. Impact of imperfect foresight on the optimal DER deployment, remuneration and policy. Appl Energy 2022;326:119885.

[2] United Nations. The UN climate change conference (COP26). 2022, URL https://www.un.org/en/climatechange/cop26. Retrieved July.

[3] Charalambous A, Hadjidemetriou L, Kyriakides E, Polycarpou MM. A coordinated voltage–frequency support scheme for storage systems connected to distribution grids. IEEE Trans Power Electron 2021;36(7):8464–75. http://dx.doi.org/10.1109/TPEL.2020.3046030.

[4] Xu L, Guo Q, He G, Jia S, Sun H. Novel properties of heterogeneous delay in inverter-based cyber–physical microgrids under fully distributed control. Appl Energy 2022;306:118102.

[5] Mejia-Ruiz GE, Arrieta-Paternina MR, Sevilla S, Rafael F, Korba P. Fast hierarchical coordinated controller for distributed battery energy storage systems to mitigate voltage and frequency deviations. Appl Energy 2022;1–20.

[6] Hanif S, Alam M, Roshan K, Bhatti BA, Bedoya JC. Multi-service battery energy storage system optimization and control. Appl Energy 2022;311:118614.

[7] Wang W, Fang X, Cui H, Li F, Liu Y, Overbye TJ. Transmission-and-distribution dynamic co-simulation framework for distributed energy resource frequency response. IEEE Trans Smart Grid 2022;13(1):482–95. http://dx.doi.org/10.1109/TSG.2021.3118292.

[8] Mejia-Ruiz GE, Cárdenas-Javier R, Arrieta Paternina MR, Rodríguez-Rodríguez JR, Ramirez JM, Zamora A. Coordinated optimal volt/var control for distribution networks via D-PMUs and EV chargers by exploiting the eigensystem realization. IEEE Trans Smart Grid 2021;12(3):2425–38. http://dx.doi.org/10.1109/TSG.2021.3050443.

[9] Wasiak I, Szypowski M, Kelm P, Mieński R, Wędzik A, Pawełek R, et al. Innovative energy management system for low-voltage networks with distributed generation based on prosumers' active participation. Appl Energy 2022;312:118705.

[10] Pearson S, Wellnitz S, Crespo del Granado P, Hashemipour N. The value of TSO-DSO coordination in re-dispatch with flexible decentralized energy sources: Insights for Germany in 2030. Appl Energy 2022;326:119905.

[11] Barbierato L, Pons E, Mazza A, Bompard EF, Rajkumar VS, Palensky P, et al. Stability and accuracy analysis of a distributed digital real-time cosimulation infrastructure. IEEE Trans Ind Appl 2022;58(3):3193–204. http://dx.doi.org/10.1109/TIA.2022.3155459.

[12] Wu W, Li P, Fu X, Yan J, Wang C. Flexible shifted-frequency analysis for multi-timescale simulations of active distribution networks. Appl Energy 2022;321:119371.

[13] Armghan H, Yang M, Ali N, Armghan A, Alanazi A. Quick reaching law based global terminal sliding mode control for wind/hydrogen/battery DC microgrid. Appl Energy 2022;316:119050.

[14] Yu H, Shang Y, Niu S, Cheng C, Shao Z, Jian L. Towards energy-efficient and cost-effective DC nanaogrid: A novel pseudo hierarchical architecture incorporating V2G technology for both autonomous coordination and regulated power dispatching. Appl Energy 2022;313:118838.

[15] Pokharel M, Ho CNM. Development of interface model and design of compensator to overcome delay response in a PHIL setup for evaluating a grid-connected power electronic DUT. IEEE Trans Ind Appl 2022;58(3):4109–21. http://dx.doi.org/10.1109/TIA.2022.3159495.

[16] Mizuta N, Kamo S, Toda H, Susuki Y, Ota Y, Ishigame A. A hardware-in-the-loop test on the multi-objective ancillary service by in-vehicle batteries: Primary frequency control and distribution voltage support. IEEE Access 2019;7:161246–54. http://dx.doi.org/10.1109/ACCESS.2019.2951748.

[17] Shang L, Dong X, Liu C, Gong Z. Fast grid frequency and voltage control of battery energy storage system based on the amplitude-phase-locked-loop. IEEE Trans Smart Grid 2022;13(2):941–53. http://dx.doi.org/10.1109/TSG.2021.3133580.

[18] Xu Y, Sun W, Qu Z. Chapter three - renewable energy integration and system operation challenge: control and optimization of millions of devices. In: Jiang H, Zhang Y, Muljadi E, editors. New technologies for power system operation and analysis. Academic Press; 2021, p. 49–98.

[19] Sadnan R, Krishnamoorthy G, Dubey A. Transmission and distribution quasi-static co-simulation: Analysis and comparison of T&D coupling strength. IEEE Access 2020;8:124007–19. http://dx.doi.org/10.1109/ACCESS.2020.3006058.

[20] Zuo Y, Yuan Z, Sossan F, Zecchino A, Cherkaoui R, Paolone M. Performance assessment of grid-forming and grid-following converter-interfaced battery energy storage systems on frequency regulation in low-inertia power grids. Sustainable Energy, Grids and Netw. 2021;27:100496.

[21] Oshnoei A, Kheradmandi M, Blaabjerg F, Hatziargyriou ND, Muyeen S, Anvari-Moghaddam A. Coordinated control scheme for provision of frequency regulation service by virtual power plants. Appl Energy 2022;325:119734.

[22] Rakhshani E, Perilla A, Torres JLR, Gonzalez-Longatt FM, Soeiro TB, Van Der Meijden MAMM. FAPI controller for frequency support in low-inertia power systems. IEEE Open Access J Power and Energy 2020;7:276–86. http://dx.doi.org/10.1109/OAJPE.2020.3010224.

[23] Riquelme-Dominguez JM, Gonzalez-Longatt F, Melo AFS, Rueda JL, Palensky P. Cyber-physical testbed co-simulation real-time: System frequency response. In: 2022 IEEE international conference on environment and electrical engineering and 2022 IEEE Industrial and commercial power systems Europe (EEEIC / I&CPS Europe). 2022, p. 1–5. http://dx.doi.org/10.1109/EEEIC/ICPSEurope54979.2022.9854592.

[24] Song X, Cai H, Jiang T, Sennewald T, Kircheis J, Schlegel S, et al. Research on performance of real-time simulation based on inverter-dominated power grid. IEEE Access 2021;9:1137–53. http://dx.doi.org/10.1109/ACCESS.2020.3016177.

[25] Xie F, McEntee C, Zhang M, Lu N, Ke X, Vallem MR, et al. Networked HIL simulation system for modeling large-scale power systems. In: 2020 52nd North American power symposium. NAPS, 2021, p. 1–6. http://dx.doi.org/10.1109/NAPS50074.2021.9449646.

[26] Estebsari A, Vogel S, Melloni R, Stevic M, Bompard EF, Monti A. Frequency control of low inertia power grids with fuel cell systems in distribution networks. IEEE Access 2022;10:71530–44. http://dx.doi.org/10.1109/ACCESS.2022.3187099.

[27] Datta U, Kalam A, Shi J. Battery energy storage system control for mitigating PV penetration impact on primary frequency control and state-of-charge recovery. IEEE Trans Sustain Energy 2020;11(2):746–57. http://dx.doi.org/10.1109/TSTE.2019.2904722.

[28] National Electrical Manufacturers Association, et al. American national standards institute (ANSI) C84.1, voltage ratings for electric power systems and equipment. 2016.

[29] Mejía Ruiz GE, Muñoz N, Cano JB. Modeling, analysis and design procedure of LCL filter for grid connected converters. In: 2015 IEEE workshop on power electronics and power quality applications. PEPQA, 2015, p. 1–6. http://dx.doi.org/10.1109/PEPQA.2015.7168215.

[30] Alghamdi B, Cañizares C. Frequency and voltage coordinated control of a grid of AC/DC microgrids. Appl Energy 2022;310:118427.

[31] Mejía-Ruiz GE, Rodríguez JR, Paternina MRA, Muñoz-Galeano N, Zamora A. Grid-connected three-phase inverter system with LCL filter: Model, control and experimental results. In: IEEE ISGT Latin America. 2019, p. 1–6.

[32] Fan L, Miao Z. Time-domain measurement-based *DQ*-frame admittance model identification for inverter-based resources. IEEE Trans Power Syst 2021;36(3):2211–21. http://dx.doi.org/10.1109/TPWRS.2020.3040360.

[33] Marks ND, Kong WY, Birt DS. Stability of a switched mode power amplifier interface for power hardware-in-the-loop. IEEE Trans Ind Electron 2018;65(11):8445–54. http://dx.doi.org/10.1109/TIE.2018.2814011.